

https://doi.org/10.1070/QEL17538

Broadband (100 kHz–100 MHz) ultrasound PVDF detectors for raster-scan optoacoustic angiography with acoustic resolution

A.A. Kurnikov, K.G. Pavlova, A.G. Orlova, A.V. Khilov,
V.V. Perekatova, A.V. Kovalchuk, P.V. Subochev

Abstract. **Spherical ultrasonic antennas are used in raster-scan optoacoustic (OA) angiography to record broadband signals generated by haemoglobin molecules in blood when they absorb pulsed optical radiation. Depending on the size of haemoglobin-containing structures, the characteristic frequencies of OA signals can vary quite significantly, ranging from hundreds of kilohertz to hundreds of megahertz. Meanwhile, the bandwidth of the receiving frequency band of standard piezoelectric sensors, as a rule, does not exceed the centre frequency value. It is possible to expand the receiving band of ultrasonic detectors to the required 0.1 kHz – 100 MHz values by using nonresonant piezomaterials based on polyvinidylene fluoride (PVDF). Two ultra-wideband detectors based on PVDF piezofilms of different thicknesses (9 μm and 25 μm) with different amplitude-frequency characteristics are experimentally compared. Comparative OA imaging of a tissue-like phantom demonstrates that the low-frequency sensor (film thickness l = 25 μm) has a greater depth of field, while the high-frequency sensor (l = 9 μm) has a better sensitivity in the range of 40–100 MHz. Using OA imaging of an experimental tumour *in vivo*, it is shown that a sensor with l = 25 μm is better suited for examining normal tissue containing relatively large blood vessels, while a sensor with l = 9 μm is better suited for studying tumour tissue containing a large number of multidirectional blood vessels of minimal size comparable to the maximum spatial resolution of the OA system.**

Keywords: *optoacoustic angiography, optoacoustic microscopy, PVDF films, model experiment, tumour angiogenesis, CT26 mouse colon carcinoma.*

1. Introduction

The pathogenesis of a number of diseases is accompanied by an imbalance of vascular growth, which can be considered as one of the main diagnostic criteria. Normally, the most active angiogenesis is observed during the period of embryonic development and healing of damaged tissues [1]. Neoangiogenesis (tumour vascularisation) promotes the growth and proliferation of malignant neoplasms and contributes to the metastatic spread of the tumour. The process of angiogenesis includes the migration and division of endothelial cells, the formation of a new basement membrane, and the organisation of tubular structures [2]. The vessels formed in the tumour tissues have a number of significant differences from the vessels of normal tissues: they are characterised by the absence of hierarchy, tortuosity and defective structure of the vascular tubes.

In the 70s of the last century, it was suggested [3] about the significance of angiogenesis in the growth of a tumour node with a volume of more than 1–2 mm^3. Subsequently, the dependence of stable growth of solid tumours on neovascularisation was proved, which changed the approach to treatment, as a result of which the main attention was focused on antiangiogenic therapy [4–6].

Understanding the process of neovascularisation as a key factor in tumour development showed the need to use diagnostic methods allowing noninvasive assessment of the structural and functional states of the vascular bed of malignant neoplasms.

The size of blood vessels in the organism can vary widely. For example, in small laboratory animals, the diameter of capillaries is several microns, while the diameter of arteries and veins reaches several hundred microns [7]. For comprehensive diagnosis of the vascular bed, it is preferable to use multiscale angiography methods capable of visualising vessels of any size, which is quite difficult for many existing angiographic methods.

Conventional CT [8] and MRI [9] angiography methods have insufficient resolution for visualisation of the capillary network. Optical coherent angiography methods have an increased penetration depth; however, significant scattering of light inside the tissue [10, 11] makes it difficult to obtain images at a depth of ~1 mm. The newest methods of optical microscopy [12] are still far from being used *in vivo*.

Ultrasound imaging systems based on the Doppler effect allow angiographic examination at a sufficient depth [13], but, as a rule, are characterised by low spatial resolution, since they cannot distinguish signals from small vessels with a low blood flow rate. Due to the similarity of the mechanical properties of the blood vessels and surrounding tissues, the implementation of the classical principles of ultrasonic location at scales less than 100 μm [14] is quite difficult.

A more versatile method for visualising the circulatory system of organisms at the level of micro- and macroscopic scales is the method of optoacoustic (OA) angiography [15, 16]. The latter is based on the conversion of absorbed light into acoustic waves, which makes it possible to obtain images

A.A. Kurnikov, K.G. Pavlova Institute of Applied Physics, Russian Academy of Sciences, ul. Ulyanova 46, 603950 Nizhny Novgorod, Russia; Lobachevsky State University of Nizhny Novgorod, prosp. Gagarina 23, 603022 Nizhny Novgorod, Russia; e-mail: 780pavlova@gmail.com;
A.G. Orlova, A.V. Khilov, V.V. Perekatova, A.V. Kovalchuk, P.V. Subochev Institute of Applied Physics, Russian Academy of Sciences, ul. Ulyanova 46, 603950 Nizhny Novgorod, Russia

Received 16 February 2021
Kvantovaya Elektronika **51** (5) 383–388 (2021)
Translated by M.A. Monastyrskiy

of haemoglobin-containing structures with optical contrast and ultrasonic resolution at depths of diffuse light propagation. The use of several optical wavelengths for OA imaging makes it possible to separate the main chromophores contained in the blood – oxy- and deoxyhaemoglobin [17, 18].

Currently, OA angiography is successfully used in experimental oncology for the analysis of tumour vascularisation during various periods of growth [19, 20] and in the course of treatment [21, 22], as well as in clinical oncology for the diagnosis of neoplasms and the development of new prognostic criteria [23].

To implement the multiscale potential of OA angiography, it is necessary to use ultrasonic antennas designed for various frequency ranges. For example, haemorrhages with a transverse size of more than 1 mm, often formed following therapeutic effects, generate ultrasound frequencies of ~0.1 MHz, while the smallest blood vessels ~15 μm in size, prevailing in the early stages of tumour growth, generate frequencies of ~100 MHz. Unfortunately, the width of the receiving frequency band of standard piezoelectric sensors is quite limited and, as a rule, does not exceed the centre frequency value [24]. It is possible to expand the receiving band of ultrasonic detectors to the required 0.1 – 100 MHz using nonresonant piezomaterials based on polyvinidylene fluoride (PVDF) [25]. The present work is dedicated to the experimental comparison of two ultrawideband detectors based on piezopolymer PVDF films of different thicknesses (9 and 25 μm), which have similar frequency reception bands with different amplitude – frequency characteristics.

2. Materials and methods

2.1. Piezopolymer PVDF films

Piezopolymer PVDF films are made in the form of sheets of various sizes and thicknesses. The relatively low acoustic impedance of PVDF compared to solid piezomaterials provides better acoustic matching of the material with water and biological tissues. The piezoelectric material itself is soft and elastic, which makes it possible to give the detectors an arbitrary geometric shape, while the low mechanical Q-factor provides the PVDF detectors with important frequency characteristics. The maximum frequency of the PVDF antenna can be defined as the ratio of the speed of sound in the film ($c \approx 2200$ m s^{-1}) to its thickness l: $f_{max} = c/l$.

The sensitivity of PVDF antennas with their identical geometry is determined by the thickness l, capacitance C and piezoelectric constant d_{33} of the film. Using the known parameters of a spherical sensor, the noise equivalent pressure (sensitivity threshold) of the detector can be determined by the formula [26]

$$\mathrm{NEP} = \frac{4}{d_{33}}\sqrt{\frac{kTC}{SS'}}, \qquad (1)$$

where S' and S are the areas of film sections for which the capacitance was measured, and the sensitivity was estimated; k is the Boltzmann constant; and $T = 300$ K.

In this work, we used piezopolymer PVDF films with a thickness of 9 and 25 μm, manufactured using the same technology by the same manufacturer (Precision Acoustics, Great Britain). The thickness of the gold electrode applied to each film was ~1 μm.

The parameters characterising the sensitivity thresholds of both films are as follows: for the PVDF-9 detector, d_{33} = 12.9 pC N^{-1}, permittivity $\varepsilon = 10$, and NEP = 8.38 Pa; for the PVDF-25 detector, d_{33} = 11.6 pC N^{-1}, $\varepsilon = 12.37$, and NEP = 6.52 Pa. To determine the NEP value, the capacitance of each of the films was measured using a GDM-8245 multimetre (GW Instek, China), while the piezoelectric constant d_{33} was measured using a PKD3-2000 piezometer (Poly-K, USA). The noise equivalent pressure (NEP) was calculated using formula (1) using the measured values C, d_{33} and the known film thickness l.

2.2. Manufacture of PVDF antennas

To manufacture the PVDF-25 and PVDF-9 detectors (with a film thickness of 25 and 9 μm), each film was given the same spherical shape. The focal length and apertures for each antenna were 6.7 and 8 mm, respectively. Each of the antennas had an internal plastic housing on which the PVDF film was attached, and an external metal housing. The grounding electrode of the film was attached to the outer housing with a conductive adhesive. In the metal housing of each antenna, an identical broadband amplifier was placed, shielded by an external housing. The scheme of the PVDF detector is shown in Fig. 1.

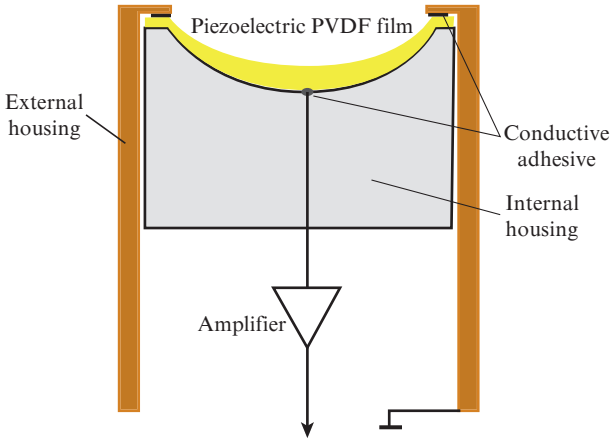

Figure 1. Scheme of the PVDF detector.

For the PVDF-25 and PVDF-9 detectors, the upper frequencies of the reception band were 88 and 244 MHz, respectively. In this case, the reception band of both antennas was additionally limited by the gain band of the matching amplifier (from 100 kHz to 100 MHz), selected from the following considerations. Lower frequency (compared to 100 kHz) OA signals were filtered because they corresponded to structures whose dimensions exceeded the scanning range (10 mm). Higher frequency (over 100 MHz) OA signals were cut off by a frequency filter due the smallness of their amplitude caused by the strong attenuation of ultrasound in water at these frequencies.

2.3. Model experiments

For quantitative comparison of the amplitude – frequency characteristics of the two antennas, we performed OA scanning of microfibres with a diameter of 7 μm and microspheres

with a diameter of 15 μm (Cospether, USA) located at different (500 and 1000 μm) depths of the tissue-mimicking phantom. A phantom medium simulating the acoustic and optical properties of biological tissue was prepared on the basis of a 1.5% aqueous solution of agar (Sigma-Aldrich, USA) and a 4% aqueous solution of lipofundin (B. Brown, Germany). The phantom was scanned in an area of 3 × 3 mm with a step of 10 μm. The characteristic bands of receiving frequencies for each of the antennas were determined from the OA spectra of the microsphere located near the acoustic focus of the sensor.

2.4. In vivo experiments

For a qualitative comparison of the angiographic capabilities of both antennas, the experimental tumour was visualised *in vivo* (the tumour was scanned in the region of 1 cm^2 with a step of 25 μm). The objects were mice of the Balb/c line inoculated with a CT26 colon carcinoma tumour (ATCC No. CRL-2638). To create a tumour model, 5×10^5 CT26 cells in 50 μL PBS were subcutaneously injected into the outer side of the left thigh. The experiments were conducted on the fifth day of the neoplasm growth. Before the examination, the hair was removed in the scanning area. During the experiment, the animals were anesthetised with 1.5% isoflurane (Laboratorios Karizoo, Spain) in 100% O_2 at a gas flow rate of 0.1 L min^{-1} using an anaesthesia breathing apparatus Zoomed Minor Vet (Zoomed, Russia). The animals were fixed on a support plate in a lateral position, and an ultrasonic gel was applied to the area of study.

The experiment was performed in accordance with the requirements of the rules and regulations governing research work on the safety and effectiveness of medicines (Order of the Ministry of Health and Social Development of the Russian Federation No. 708-n of 23.08.2010), as well as international legal norms and ethical codes for the experimental use of animals (NIH Publications No. 8023, revised in 1978).

2.5. Optoacoustic setup

The scanning system of OA microscopy (Fig. 2) was similar to those used in [27, 28]. During OA experiments, the optical pulses were generated by a Wedge HB laser (Bright Solutions, Italy) (wavelength 532 nm; pulse repetition rate 2 kHz, and pulse duration 1 ns). The laser radiation was delivered to the study area using a fibre-optic bundle (CeramOptec, Germany), into which the compared PVDF-9 and PVDF-25 detectors were subsequently inserted. The optical fibres were arranged

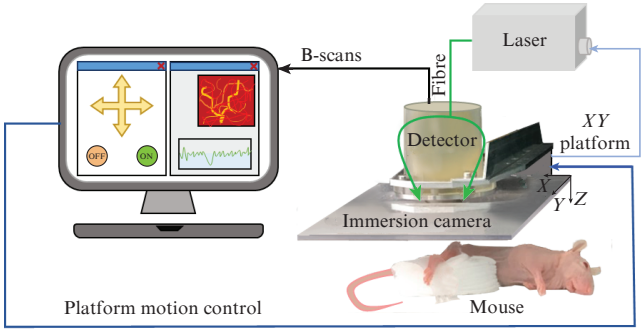

Figure 2. Scheme of scanning optoacoustic microscopy.

so that the probe beams intersected at the focal waist of a single-element acoustic detector [29]. Electrical signals from PVDF detectors were digitised by a Razor16 two-channel 16-bit analogue-to-digital converter (GaGe, USA) with a sampling rate of 200 MHz. To obtain a three-dimensional image, the assembled OA probe was placed on two linear platforms M-664 (PImicos, Germany) and LS-40 (PImicos, Germany), which provided mechanical scanning in the *XY* plane.

2.6. Data processing and presentation

For all B-scans of unprocessed 3D data sets, two-dimensional Fourier reconstruction [30] was performed sequentially in two mutually perpendicular planes [31], separately for three frequency ranges: 0.1–5 MHz (range I), 5–40 MHz (range II), and 40–100 MHz (range III). Data corresponding to different frequencies was processed using Avizo (Thermo Scientific) software. The characteristic dimensions of the objects were estimated by the ratio of the speed of sound in biological tissues ($c \approx 1500$ m s^{-1}) to the frequency received by the detector. For the given frequency ranges, the object dimensions were 15–0.3 mm (range I), 300–37.5 μm (II), and 37.5–15 μm (III).

3. Results and discussion

Figure 3 shows the results of reconstruction of three-dimensional data sets obtained by the PVDF-9 and PVDF-25 detectors. The phantom image is displayed in the frequency ranges I, II, and III.

The phantom images (Fig. 3) demonstrate differences in the amplitude–frequency characteristics of the detectors in the same frequency ranges. Thus, due to the significantly higher sensitivity of the antenna at low frequencies (0.1–5 MHz), the PVDF-25 detector provided a greater depth of field (1.5 mm) than the PVDF-9 detector (1 mm). At medium frequencies (5–40 MHz), the antennas exhibited similar sensitivity, spatial resolution and depth of field. At high frequencies (40–100 MHz), the PVDF-9 detector's antenna visualised a thin phantom structure with higher (compared to PVDF-25) sensitivity and spatial resolution.

The operating frequency bands of the PVDF-25 and PVDF-9 detectors at a 0.01 level were 56.5 and 96.5 MHz, respectively. It can be seen from Fig. 4a that in the high frequency range (40–100 MHz), a plateau is observed in the PVDF-9 detector's spectrum at a level of 1%–10% of the signal maximum, which makes it possible to obtain images of the smallest (10 μm) objects. Figure 4b shows the SNRs for three frequency ranges, which allow us to quantitatively compare the frequency characteristics of the detectors' antennas. The SNR value is determined by the formula

$$\mathrm{SNR} = 10\lg\left(\frac{\max(\mathrm{OA}_{\mathrm{signal}})}{\langle \mathrm{std}(\mathrm{OA}_{\mathrm{noise}})\rangle_{N=100}}\right).$$

Here $\max(\mathrm{OA}_{\mathrm{signal}})$ is the maximum signal value from a three-dimensional data set for each frequency range; and $\langle \mathrm{std}(\mathrm{OA}_{\mathrm{noise}})\rangle_{N=100}$ is the root-mean-square deviation of the noise averaged over 100 OA A-scans, which was also determined for each frequency range.

Figures 5 and 6 display the results of *in vivo* compression of both detections reflecting the advantages and disadvantages of comparative amplitude–frequency characteristics of the detectors. In the image obtained using the PVDF-25

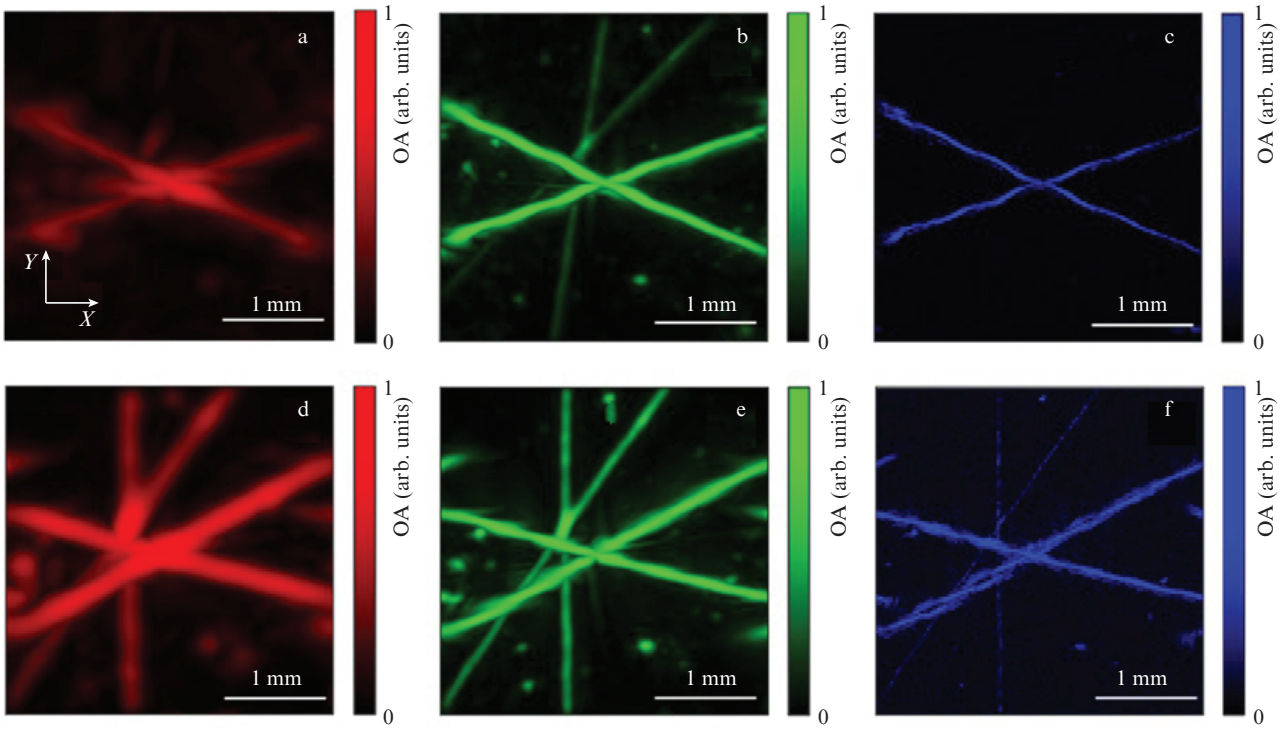

Figure 3. (Colour online) OA imaging of the phantom using (a–c) PVDF-9 and (d–f) PVDF-25 detectors. The images were reconstructed for the frequency ranges (a, d) 0.1–5 MHz, (b, e) 5–40 MHz, (c, f) 40–100 MHz.

detector (Figs 5d–5f), the vascular network of surface tissues is distinguishable – a hierarchy of the network is visible, and the differentiation of the sizes of vessels and their shape is visualised. However, the tumour's circulatory system represented by smallest blood vessels is poorly visualised by the PVDF-25 antenna, which is associated with its relatively low spectral sensitivity at frequencies above 50 MHz (see Fig. 4a).

The images in the three frequency ranges, obtained using the PVDF-9 detector have more significant differences. First of all, a clearly discernible tumour node is observed in all frequency ranges (Figs 5a–5c). At low frequencies, the tumour is an undifferentiated accumulation of haemoglobin and only the largest vessels of normal tissues are visible. The same vessels (along with small veins and arteries) are visualised in more detail in the range of 5–40 MHz. Switching to the high-frequency (40–100 MHz) range makes it possible to obtain contrast images of the smallest capillaries of the tumour tissue. The visualised structure of the tumour vessels may be the result of the specific structure of the blood vessels of the CT26 tumour at this stage of growth: sinusoids are present in the wall of tortous capillaries [32], i.e. large openings, the size of which allows red blood cells and some proteins to freely exit the vascular tube into the parenchyma.

The partial 'absence' of blood vessels in the tumour in visualisation using the PVDF-25 detector antenna could however be associated with a different degree of pressing the tumour to the immersion chamber, since the experimental setup used did not provide for pressure control [33]. A sufficiently strong pressing force (which we tried to avoid in this experiment) could affect the blood filling of vessels placed in direct contact with the immersion chamber (especially the smallest tumour vessels).

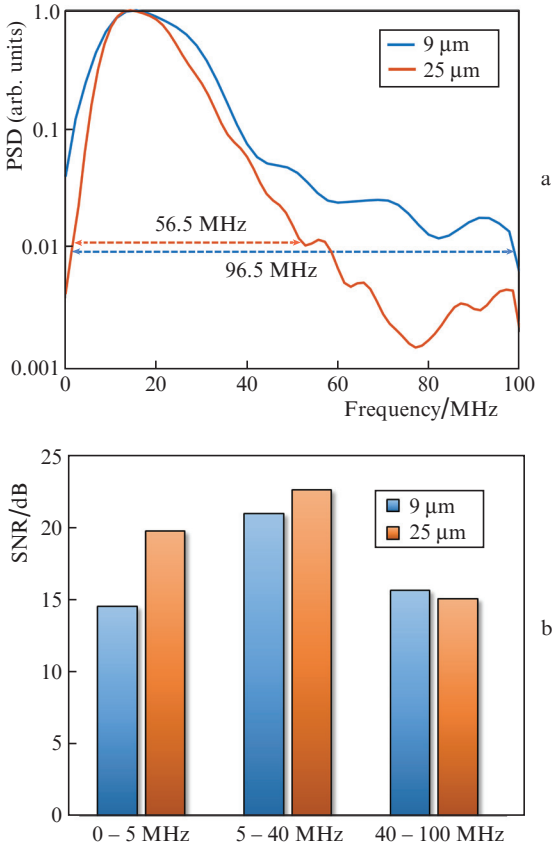

Figure 4. (Colour online) Frequency characteristics of PVDF detectors: (a) power spectral density (PSD) and (b) signal-to-noise ratio (SNR) for three frequency ranges.

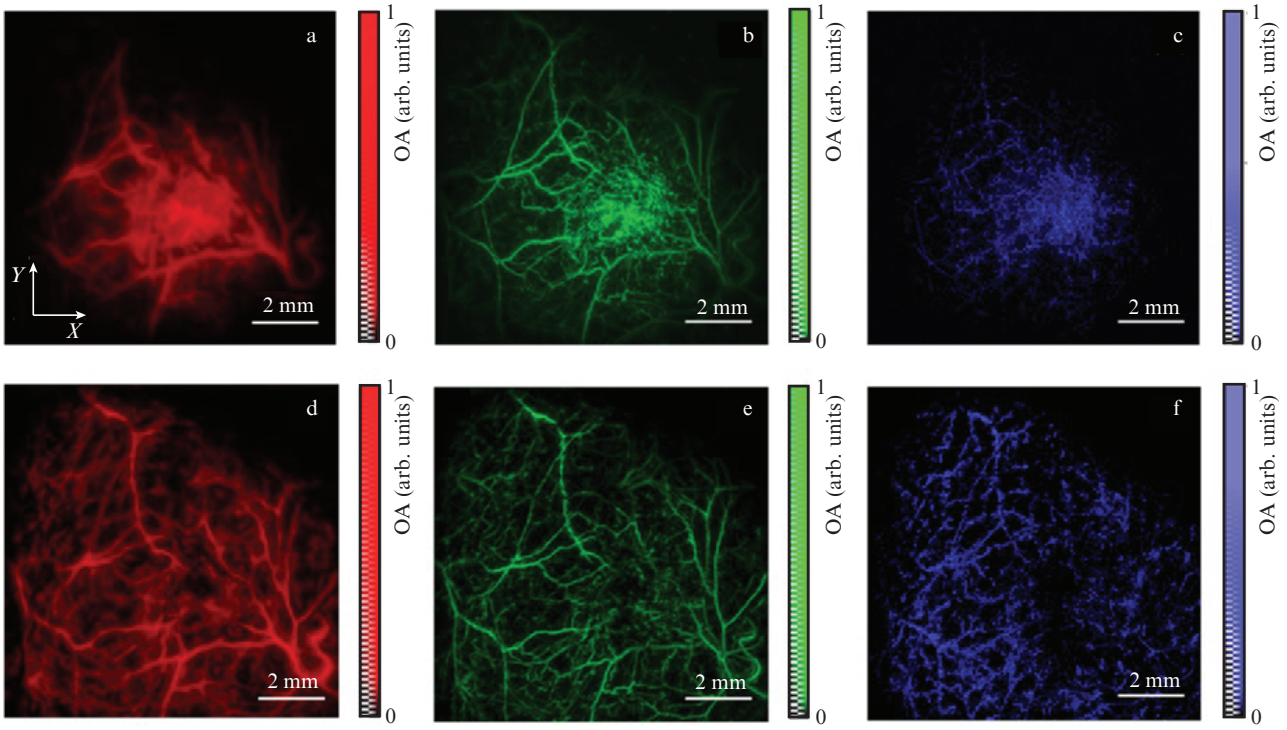

Figure 5. (Colour online) OA imaging of mouse tumours using (a–c) PVDF-9 and (d–f) PVDF-25 detectors. The images were reconstructed for the frequency ranges (a, d) 0.1–5 MHz, (b, e) 5–40 MHz, (c, f) 40–100 MHz.

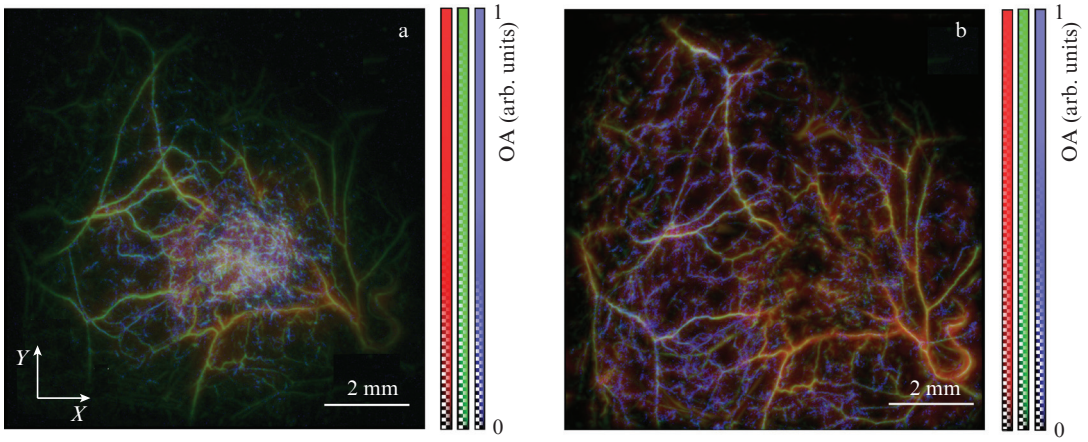

Figure 6. (Colour online) Broadband OA imaging of mouse tumours using (a) PVDF-9 and (b) PVDF-25 detectors.

Vascularisation of normal tissues is strictly organised and represents an ordered system of the circulatory bed [34]. The diameter of arteries, veins, and capillaries in normal tissues of Balb/c mice is 150, 250, and 4 μm, respectively [7]. The tumour blood network has a disturbed hierarchy, specific shape and structure. In work [32], using morphological methods, it was shown that on the fifth day of the CT26 colon carcinoma growth, single sinusoidal vessels are formed, whose size varies from 7 to 20 μm, which is comparable to the size of arterioles and venules of a healthy muscle (18 μm/14 μm) [7]. In this work, the CT26 vascular system was visualised by means of an intravital noninvasive method. However, since the circulatory bed at this relatively early stage of neoplasm development is mainly represented by newly formed small vessels, it is preferable to use the PVDF-9 detector's antenna for tumour imaging.

4. Conclusions

The optoacoustic study of the microcirculatory bed using ultra-wideband PVDF-25 and PVDF-9 detectors made it possible to conduct multiscale diagnosis of vessels with a diameter of 30 to 200 μm. For detailed imaging of vessels of different diameters, the signal from both OA sensors was divided into three frequency ranges: low (0.1–5 MHz), medium (5–40 MHz), and high (40–100 MHz). A direct comparison of the sensors showed that the PVDF-25 detector is more preferable for OA angiography of normal tissues, providing a greater depth of field due to its increased sensitivity at frequencies of 0.1–40 MHz. For angiography of experimental neoplasms, the PVDF-9 detector antenna made of a thinner (9 μm) PVDF film and having an increased sensitivity in the frequency range of 40–100 MHz proved to

be the most informative for studying the vascular microstructure of neoangiogenesis.

Acknowledgements. The work was supported by the Centre of Excellence "Center of Photonics" funded the Ministry of Science and High Education of the Russian Federation (Agreement No. 075-15-2020-906). The authors thank A.B. Volovetsky for the provided tumour models.

References

1. Carmeliet P. *Nature*, **438**, 932 (2005).
2. Kuol N., Stojanovska L., Apostolopoulos V., Nurgali K. *Cancer Microenviron.*, **11**, 1 (2018).
3. Folkman J. *Annals Surgery*, **175**, 409 (1972).
4. Li T., Kang G., Wang T., Huang H. *Oncol. Lett.*, **16**, 687 (2018).
5. Leunig M., Yuan F., Menger M., Boucher Y., Goetz A., Messmer K., Jain R. *Cancer Res.*, **52**, 23 6553 (1992).
6. Folkman J. *Nat. Rev. Drug. Discov.*, **6**, 273 (2007).
7. Müller B., Lang S., Dominietto M., Rudin M., Schulz G., Deyhle H., Germann M., Pfeiffer F., David C., Weitkamp T. *Proc. SPIE*, **7078**, 70780B (2008).
8. Schambach S.J., Bag S., Schilling L., Groden C., Brockmann M.A. *Methods*, **50**, 2 (2010).
9. Johnson G.A., Cofer G.P., Gewalt S.L., Hedlund L.W. *Radiology*, **222**, 789 (2002).
10. Matveev L.A., Zaitsev V.Yu., Gelikonov G.V., Matveyev A.L., Moiseev A.A., Ksenofontov S.Yu., Gelikonov V.M., Sirotkina M.A., Gladkova N.D., Demidov V., Vitkin A. *Opt. Lett.*, **40**, 1472 (2015).
11. Orlova A.G., Subochev P.V., Moiseev A.A., Smolina E.O., Ksenofontov S.Yu., Kirillin M.Yu., Shakhova N.M. *Quantum Electron.*, **49**, 25 (2019) [*Kvantovaya Elektron.*, **49**, 25 (2019)].
12. Gigan S. *Nature Photon.*, **11** (1) 14 (2017).
13. Hwang J.Y. *Ultrasonography*, **36**, 111 (2017).
14. Kumagai K., Koike H., Nagaoka R., Sakai S., Kobayashi K., Saijo Y. *Ultrasound Med., Biol.*, **38**, 1833 (2012).
15. Wang L.V., Yao J. *Nat. Methods*, **13**, 627 (2016).
16. Khokhlova T.D., Pelivanov I.M., Karabutov A.A. *Acoust. Phys.*, **55**, 674 (2009).
17. Luís Deán-Ben X., Razansky D. *Light Sci. Appl.*, **3**, e137 (2014).
18. Perekatova V.V., Subochev P.V., Kirillin M.Y., Sergeeva E.A., Kurakina D.A., Orlova A.G., Postnikova A.S., Turchin I.V. *Laser Phys. Lett.*, **16**, 116201 (2019).
19. Orlova A., Sirotkina M., Smolina E., Elagin V., Kovalchuk A., Turchin I., Subochev P. *Photoacoustics*, **13**, 25 (2019).
20. Lin R., Chen J., Wang H., Yan M., Zheng W., Song L. *Quant. Imaging Med. Surg.*, **5**, 23 (2015).
21. Haedicke K., Agemy L., Omar M., Berezhnoi A., Roberts S., Longo-Machado C., Skubal M., Nagar K., Hsu H.T., Kim K., Reiner T., Coleman J., Ntziachristos V., Scherz A., Grimm J. *Nat. Biomed.*, **4**, 286 (2020).
22. Zhou H.C., Chen N., Zhao H., Yin T., Zhang J., Zheng W., Song L., Liu C., Zheng R. *Photoacoustics*, **15**, 100143 (2019).
23. Toi M., Asao Y., Matsumoto Y., Sekiguchi H., Yoshikawa A., Takada M., Kataoka M., Endo T., Kawaguchi-Sakita N., Kawashima M., Fakhrejahani E., Kanao S., Yamaga I., Nakayama Y., Tokiwa M., Torii M., Yagi T., Sakurai T., Togashi K., Shiina T. *Sci. Rep.*, **7**, 1 (2017).
24. Ku G., Wang X., Stoica G., Wang L.V. *Phys. Med. Biol.*, **49**, 1329 (2004).
25. Subochev P., Prudnikov M., Vorobyev V., Postnikova A., Sergeev E., Perekatova V., Orlova A., Kotomina V., Turchin I. *J. Biomed. Opt.*, **23**, 1 (2018).
26. Oraevsky A.A., Karabutov A.A. *Proc. SPIE*, **3916**, 228 (2000).
27. Subochev P., Katichev A., Morozov A., Orlova A., Kamensky V., Turchin I. *Opt. Lett.*, **37**, 4606 (2012).
28. Subochev P. *Opt. Lett.*, **41**, 1006 (2016).
29. Subochev P., Fiks I., Frenz M., Turchin I. *Laser Phys. Lett.*, **13**, 025605 (2016).
30. Spadin F., Jaeger M., Nuster R., Subochev P., Frenz M. *Photoacoustics*, **17**, 100149 (2020).
31. Perekatova V.V., Kirillin M.Yu., Turchin I.V., Subochev P.V. *J. Biomed. Opt.*, **23**, 1 (2018).
32. Kuznetsov S.S., Snopova L.B., Karabut M.M., Sirotkina M.A., Buyanova N.L., Kalganova T.I., Elagin V.V., Senina-Volzhskaya I.V., Barbashova L.N., Zagainova E.V., Vitkin A., Gladkova N.D. *Sovrem. Tehnol. Med.*, **7**, 32 (2015).
33. Anosov A.A., Kirillin M.Y., Orlova A.G., Erofeev A.V., Sharakshane A.S., Shcherbakov M.I., Sergeeva E.A., Saijo Y., Subochev P.V. *Laser Phys. Lett.*, **17**, 085601 (2020).
34. Viallard C., Larrivée B. *Angiogenesis*, **20**, 409 (2017).